A Linear Theory of Orographic Precipitation

Ronald B. Smith and Idar Barstad

Department of Geology and Geophysics, Yale University, New Haven, Connecticut

ABSTRACT

A linear theory of orographic precipitation is developed, including airflow dynamics, condensed water advection, and downslope evaporation. The formulation extends the widely used ''upslope'' model. Vertically integrated steady-state governing equations for condensed water are solved using Fourier transform techniques. Closed form expressions are derived for special cases. For more general cases, the precipitation field is computed quickly by multiplying the terrain transform by a wavenumber-dependent transfer function.

Five length scales are included in the model: mountain width, a buoyancy wave scale, the moist layer depth, and two condensed water advection distances. The efficiency of precipitation in the model is sensitive to the decay of the forced ascent through the moist layer and to the advection of condensed water downwind into the region of descent. The strong influence of horizontal scale on precipitation pattern and amount predicted by the model is discussed. The model is illustrated by applying it to the Olympic Mountains in Washington State.

1. Introduction

The distribution of precipitation in complex terrain has usually been estimated using one of two methods: the interpolation of rain gauge station data and the so-called upslope method. In the former method, sparse station data are interpolated using inverse distance weighting or spline fitting, sometimes including an altitude or aspect correction (Daly et al. 1994; Hutchinson 1998). No influence of horizontal scale is included. In the latter method, the terrain slope and wind speed are used to estimate the condensation rate above the terrain (Collier 1975; Rhea 1978; Smith 1979; Neiman et al. 2002). Precipitation is computed from the assumption that condensed water falls immediately to the ground. Again, physical scale is not taken into account.

Several quasi-analytic models have included scale-dependent processes. Hobbs et al. (1973) and Bader and Roach (1977) have described raindrop/snow fall speeds and washout of cloud water. More recently, Alpert and Shafir (1989), Sinclair (1994), and Smith (2003a, hereafter S03) have included the advection of hydrometeors in their upslope models. The drift distances in these models, from 5 to 25 km, improve the agreement with station and radar data.

Simple upslope-advection models such as S03 have two limitations. First, they assume that the terrain-induced vertical air velocity penetrates upward through the moist layer without change. In fact, it is known from mountain wave theory that such motions may either decay or oscillate with altitude, depending on the horizontal scale and aspect ratio of the terrain and the static stability and wind speed in the environment. In either case, the upslope estimate may far exceed the actual condensation rate. Fraser et al. (1973), Durran and Klemp (1982b), and Kuligowski and Barros (1999) discuss the role of moist wave dynamics in a vertical plane.

A second problem relates to leeside descent. In upslope models, it is usually assumed that only upslope regions influence precipitation. With instantaneous conversion and fallout, the windward slope receives rain while the flat and downslope regions are dry. When time delays are included, the upslope condensate is distributed downstream, without regard for local terrain. This approach neglects the evaporation of cloud water and hydrometeors caused by descending air. The total precipitation is overestimated by this assumption. Models such as Alpert and Shafir's introduce an adjustable coefficient to reduce the prediction into a reasonable range.

The errors induced by these two problems are strongly scale dependent. For smooth hills with scales of 100 km, the upslope estimates are usually quite reasonable. On the other hand, when the terrain is rising and falling with scales of 20 km or less, both assumptions fail and the model can overestimate the total precipitation by a factor of 5 or greater. In the Italian Alps, Smith et al. (2003) showed that the upslope rainfall estimate exceeded the incoming moisture flux, an obvious violation of water conservation. The scale dependence of these errors means that the investigator must smooth the ter-

Corresponding author address: Prof. Ronald B. Smith, Dept. of Geology and Geophysics, Yale University, P.O. Box 208109, New Haven, CT 06520-8109.
E-mail: ronald.smith@yale.edu

rain by an "appropriate" amount before applying the model. The choice of smoothing scale introduces an arbitrary factor into the analysis.

Full numerical mesoscale models are now being used frequently to predict orographic precipitation. These models are replete with physical scales, in both the governing equations and the parameterizations. Numerical models are difficult to fully diagnose, however, because of their complexity and slow execution speed. Usually, less than 100 runs can be carried out to investigate their properties. Bruintjes et al. (1994), Miglietta and Buzzi (2001), Jiang (2003), and Smith et al. (2003) have been partially successful in diagnosing model behavior, but their range of parameter values was sharply restricted.

The goal of this paper is to develop a model of orographic precipitation with the following characteristics:

• analytically tractable so that its properties can be easily understood;
• applicable to actual complex terrain and arbitrary wind direction so that it can be tested against real data;
• reduces to the classical upslope model so that it can be compared with earlier work;
• includes the basic physical elements: airflow dynamics, condensed water conversion, advection and fallout, and downslope evaporation, leading to a theory of precipitation efficiency.

The first criterion suggests that our model should be mathematically linear. The challenge is to retain linearity while satisfying the other three criteria. Problems of cloud formation do not lend themselves to linear formulation because of the threshold nature of water vapor saturation (e.g., Barcilon et al. 1980; Durran and Klemp 1982b; Barcilon and Fitzjarrald 1985). Linear models must also ignore other nonlinearities such as moist airflow blocking (Jiang 2003) and cloud physics bifurcations (Jiang and Smith 2003). Nevertheless, we expect that our model will have a substantial domain of applicability.

The development of the model is described in four parts. In section 2, the equations for advection, conversion, and fallout of condensed water are introduced. In section 3, the role of airflow dynamics is discussed, following classical 3D mountain wave theory. In section 4, a treatment of evaporation and precipitation efficiency is formulated. In section 5, the combined effects of all these processes are discussed. The last two sections of the paper consider applications. In section 6, the influence of topographic scale is summarized. In section 7, we display the properties of the linear model with real terrain. The appendix describes our thermodynamic formulation.

2. Governing equations for advection, conversion, and fallout

In this section, we formulate a system of equations that describes the advection of condensed water by the mean wind.
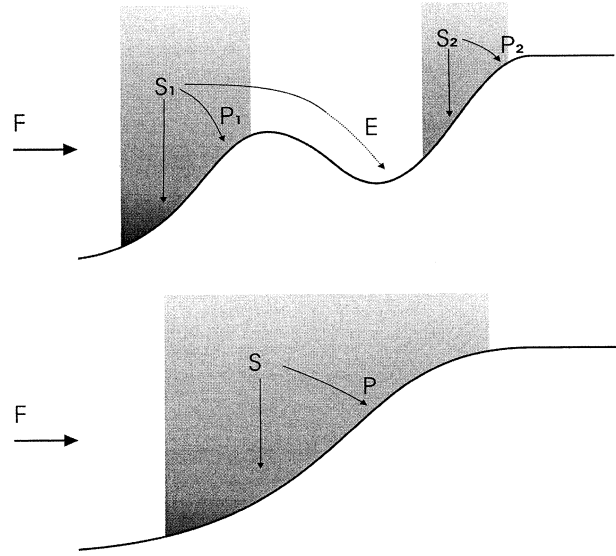

FIG. 1. A schematic illustration of water budget on a windward slope with incoming flux (F), upslope condensation source (S in the shaded region) and precipitation (P). (top) Multiscale rise; (bottom) smooth rise.

a. Formulation

The physical system that we envision is shown in Fig. 1, with a distributed source of condensed water [$S(x, y)$] arising from forced ascent. While conventional "upslope" models assume instantaneous fallout of condensed water, we allow delays and downstream advection. We begin, following Smith (S03), by postulating a pair of steady-state advection equations describing the vertically integrated cloud water density [$q_c(x, y)$] and hydrometeor density [$q_s(x, y)$].

$$\frac{Dq_c}{Dt} \approx \mathbf{U} \cdot \boldsymbol{\nabla} q_c = S(x, y) - \frac{q_c}{\tau_c} \qquad (1)$$

$$\frac{Dq_s}{Dt} \approx \mathbf{U} \cdot \boldsymbol{\nabla} q_s = \frac{q_c}{\tau_c} - \frac{q_s}{\tau_f}, \qquad (2)$$

where τ_c is the time constant for conversion from cloud water to hydrometeors (i.e., rain or snow) and τ_f is the time constant for hydrometeor fallout. The physics of conversion and fallout in orographic clouds was discussed by Hobbs et al. (1973), Rauber (1992), and others. As our model is vertically integrated, we use average values of the time constants, representative of the whole column. Estimates of the time constants range from 200 to 2000 s (Jiang and Smith 2003; Smith et al. 2003). The advecting wind vector $\mathbf{U} = U\mathbf{i} + V\mathbf{j}$ is assumed to be independent of time and space.

In (1), $S(x, y)$ is the sum of a background rate of cloud water generation and local variations created by terrain-forced uplift. A simple proposal for $S(x, y)$ is the upslope model

$$S(x, y) = S_\infty + C_w \mathbf{U} \cdot \boldsymbol{\nabla} h(x, y), \qquad (3)$$

where $C_w = \rho_{S_{ref}}(\Gamma_m/\gamma)$ is the coefficient relating condensation rate to vertical motion (see the appendix), $h(x, y)$ is the terrain, and S_∞ is the background nonorographic large-scale vertically integrated condensation rate. Equation (3) assumes saturated conditions and a terrain-forced vertical air velocity $w(x, y) = \mathbf{U} \cdot \nabla h(x, y)$ that is independent of altitude. The final term in (1) is the conversion of cloud water to hydrometeors. It appears as a source term in (2). The final term in (2) is the loss of hydrometeors associated with precipitation

$$P(x, y) = q_s(x, y)/\tau_f. \tag{4}$$

To avoid the complexity of the full orographic precipitation problem, we have reduced the problem by dealing only with vertically integrated quantities and two "lumped" categories of condensed water.

To clarify the properties of (1)–(4), we consider three trivial solutions. First, in the absence of terrain $h(x, y)$, the uniform source S_∞ will create constant values of cloud water column density ($q_c = S_\infty \tau_c$), hydrometeor column density ($q_s = S_\infty \tau_f$), and precipitation ($P_\infty = S_\infty$). Because our equations are linear, the background precipitation can be added to any orographic component.

Second, in the special case of $S_\infty = 0$ and $\tau_c = \infty$ (i.e., no conversion), (1) and (3) can be integrated to give $q_c(x, y) = C_w h(x, y)$ and $q_s = 0$, indicating the existence of cloud water over high terrain, but no precipitation. We call this the "lenticular" solution as steady clouds exist over each mountain peak with equal condensation and evaporation at their leading and trailing edges.

Third, if $S_\infty = 0$ and $\tau_f = \infty$ (i.e., no fallout), forward and reverse conversion can occur but the total condensed water behaves simply; that is, $q_c + q_s = C_w h(x, y)$. Rainwater can be created but then it is stored in the parcel until, upon descent, negative S drives q_c negative, which in turn evaporates q_s. See section 4 for further discussion of evaporation.

To obtain the general solution for the orographic precipitation, we Fourier transform (1), (2) in the two horizontal directions (S03). After some simple algebra, we obtain an expression for the Fourier transform of the precipitation distribution

$$\hat{P}(k, l) = \frac{\hat{S}(k, l)}{(1 + i\sigma\tau_c)(1 + i\sigma\tau_f)} \tag{5}$$

in terms of the specified source function. In (5), (k, l) are the components of the horizontal wavenumber vector and $\sigma = Uk + Vl$ is the intrinsic frequency (see also Smith 2003b for examples of solving the advection equation with Fourier methods). The transform (5) can be inverted to obtain the precipitation distribution $P(x, y)$ using

$$P(x, y) = \iint \hat{P}(k, l)e^{i(kx+ly)} \, dk \, dl. \tag{6}$$

According to (5), (6), precipitation is distributed downwind of each source region over a distance given by the product of wind speed and the cloud time constant. An important property of (5), (6) is that, if $S(x, y)$ is positive definite, so is $P(x, y)$. This property is proven in the next subsection. In section 4, we extend the definition of q_c to include negative values. A second property of (5), (6) is that, if $\tau_c = \tau_f = 0$ (i.e., fast conversion and fallout), then $\hat{P}(k, l) = \hat{S}(k, l)$ and thus $P(x, y) = S(x, y)$.

b. Response to a point source

The properties of (5) and (6) can be illustrated by writing the solution to a point source of condensation $S(x, y) = B\delta(x)\delta(y)$ in axis-parallel flow; for example, $U > 0$, $V = 0$. In applied mathematics, such a solution is called the Green's function. From (5), (6), using contour integration and the residue theorem,

$$P(x, y) = B\delta(y)\left[\frac{e^{-x/U\tau_c} - e^{-x/U\tau_f}}{U(\tau_c - \tau_f)}\right]. \tag{7}$$

Formula (7) is a positive definite function that rises to a maximum some distance downwind of the input pulse and then decays farther downwind. If one of the time constants is zero, (7) becomes

$$P(x, y) = B\delta(y)e^{-x/U\tau}/(U\tau). \tag{8}$$

If the two time constants are equal, using L'Hospital's rule, (7) becomes

$$P(x, y) = B\delta(y)xe^{-x/U\tau}/(U\tau)^2 \tag{9}$$

that peaks at a distance $U\tau$ downstream of the source. While (3), (5) represents a convenient model for distributing precipitation downstream, it has two serious disadvantages. First, if only positive values of S are retained, every upslope source region causes a swath of precipitation with perfect efficiency. Smith et al. (2003) showed that, for complex terrain, this approach can seriously overestimate the precipitation. The same water molecules are lifted repeatedly and, according to (3), (5), every lifting event produces precipitation. With such a model, reasonable total precipitation estimates can be achieved only by smoothing the terrain to 30 km or more so that multiple lifting is minimized.

The second problem with (3), (5) is that it takes no account of airflow dynamics: including phenomena such as lateral influence of terrain, upwind tilt of the forced ascent, and the decay of forced ascent aloft.

3. Airflow dynamics and the condensed water source term

In this section we examine the effect of airflow dynamics on the vertically integrated condensation rate.

a. Formulation

To improve the calculation of the source term in (1), we extend (3) by allowing the vertical velocity to vary as a function of altitude. The vertical integral of the condensation rate is, from (A8)

$$S(x, y) = \left(\frac{C_w}{H_w}\right) \int_0^\infty w(x, y, z)e^{-z/H_w} \, dz, \qquad (10)$$

where C_w is the thermodynamics uplift sensitivity factor (see appendix) and H_w is the depth of the moist layer. To describe the dynamics of forced ascent, we use well-known results from linear Boussinesq mountain wave theory (e.g., Queney 1947; Sawyer 1962; Smith 1979, 2002; Wurtele et al. 1996). For each Fourier component (k, l), the vertical velocity takes a complex exponential form

$$\hat{w}(k, l, z) = \hat{w}(k, l, 0)e^{imz}, \qquad (11)$$

where the vertical wavenumber is given by

$$m(k, l) = \left[\left(\frac{N_m^2 - \sigma^2}{\sigma^2}\right)(k^2 + l^2)\right]^{1/2}. \qquad (12)$$

The use of moist stability has been widely discussed in the literature (Lalas and Einaudi 1973; Fraser et al. 1973; Durran and Klemp 1982a), and recently quantitatively supported by the calculations of Jiang (2003).

In (12), the proper root must be taken to satisfy a decay or radiation condition. With weak stratification ($N_m^2 \ll \sigma^2$), the airflow is irrotational and $m = i(k^2 + l^2)^{1/2}$. In the hydrostatic limit ($N_m^2 \gg \sigma^2$), (12) reduces to

$$m(k, l) = \left[\left(\frac{N_m^2}{\sigma^2}\right)(k^2 + l^2)\right]^{1/2} \text{sgn}(\sigma). \qquad (13)$$

In the 2D hydrostatic case, $l = 0$, and $\sigma = Uk$ so that (13) reduces to

$$m(k) = \frac{N_m}{U} \text{sgn}(k). \qquad (14)$$

Substituting (11) into the transform of (10) gives

$$\hat{S}(k, l) = \hat{w}_0(k, l)\left(\frac{C_w}{H_w}\right) \int_0^\infty e^{-z/H_w}e^{imz} \, dz$$

$$= \frac{C_w\hat{w}_0(k, l)}{(1 - imH_w)}. \qquad (15)$$

Using $\hat{w}_0(k, l) = \hat{w}(k, l, 0) = i\sigma\hat{h}(k, l)$ from mountain wave theory, (15) yields a transfer function relating the transform of the terrain and the condensed water source function

$$\hat{S}(k, l) = \frac{C_w i\sigma\hat{h}(k, l)}{(1 - imH_w)}. \qquad (16)$$

In the denominator of (16), the square bracket contains the effect of vertical velocity variations up through the moist layer. If $\sigma^2 > N_m^2$ in (12), m is positive imaginary and the forced ascent decays with height. The denominator of (16) is real, positive, and greater than unity, reducing the amount of condensation. If the static stability (N) is large or the intrinsic frequency σ is small, m will be real. In this case, the vertical structure oscillates with height and partial cancellation occurs. The denominator of (16) is complex with a magnitude exceeding unity. Again, the total condensation is reduced. In both these cases, the depth of the moist layer (H_w) plays a key role. Only if $|mH_w| \ll 1$, will the vertical motion penetrate through the moist layer without shift or decay.

The effect of static stability enters several ways in (16). For example, an increased static stability (i.e., a smaller magnitude of γ) increases the available water vapor (C_w and H_w), but decreases the depth of the lifting [i.e., an increased m from (A13) and (12)].

In the following subsections we examine five different examples of how airflow dynamics influences cloud water condensation.

b. Sinusoidal terrain

The properties of (16) can be illustrated in two dimensions by considering a sinusoidal terrain with wavelength (λ), specified by

$$h(x) = \text{Re}(Ae^{ikx}), \qquad (17)$$

where $k = 2\pi/\lambda$. If the coefficient A is real, (17) is $h(x) = A\cos(kx)$. Equation (17) can be used directly in (16), using generalized functions, to give

$$S(x) = C_wU \, \text{Re}\left[\frac{ikAe^{ikx}}{1 - im(k)H_w}\right]. \qquad (18)$$

We now will examine specific values of m. In the irrotational case (12) gives $m = i|k|$, so the vertically integrated condensation is, from (18)

$$S(x) = \frac{C_wkU}{1 + |k|H_w} \, \text{Re}(Aie^{ikx}). \qquad (19)$$

According to (19), the condensation occurs directly over the windward slope. Even though the terrain slope increases by increasing k, the condensation rate does not increase significantly as the increasing terrain slope is cancelled by the decreasing penetration.

In the special case of $N_m = Uk$, the vertical wavenumber is $m = 0$ [from (12)] and complete penetration occurs; that is, from (18)

$$S(x) = C_wkU \, \text{Re}(Aie^{ikx}) \qquad (20)$$

in agreement with (3). If A is real, $S(x) = -C_wkUA \sin(kx)$.

With hydrostatic dynamics (15), the vertically integrated condensation is

$$S(x) = \frac{C_w k U}{(1 + \hat{H}^2)} \text{Re}[Ai(1 + i\hat{H})e^{ikx}], \qquad (21)$$

where $\hat{H} = N_m H_w / U$ is the nondimensional moist layer depth. If the coefficient A is real, (21) can be written

$$S(x) = \frac{-C_w k U A}{(1 + \hat{H}^2)}[\sin(kx) + \hat{H}\cos(kx)]. \qquad (22)$$

The function (22) exhibits an upstream shift and a reduced amplitude compared to the simple upslope model (20). If the moist layer depth is small, (22) reduces to the upslope model (20).

We can define a dynamical precipitation efficiency as the ratio of the actual source to the source assuming complete penetration of the forced ascent through the moist layer. Taking the magnitude of (21) and normalizing with (20)

$$\text{PE}_{\text{dyn}} = \frac{|S|}{|S_{\hat{H}=0}|} = (1 + \hat{H}^2)^{-1/2}. \qquad (23)$$

The quantity $\hat{H}$ can be interpreted as the ratio of the moist layer depth to the penetration depth of the forced ascent $d = U/N_m$. A typical value for

$$\hat{H} = (0.005 \text{ s}^{-1})(3000 \text{ m})/(15 \text{ m s}^{-1}) = 1.0$$

so that (23) gives $\text{PE}_{\text{dyn}} = 2^{-1/2} = 71\%$. If $\hat{H} \gg 1$, the forced ascent is only felt by a small lower part of the moist layer, and the net condensation is very small ($\text{PE}_{\text{dyn}} \ll 1$).

c. Rise to a plateau

In a second example, we consider a smooth rise in terrain given by the inverse tangent function $h(x) = (A/\pi)\tan^{-1}(x/a)$, with total rise $\Delta h = A$. The vertical velocity near the ground is

$$w_0(x) = U\frac{dh}{dx} = \frac{UAa}{\pi(x^2 + a^2)}, \qquad (24)$$

so

$$\hat{w}_0(k) = \frac{1}{2\pi}\int_{-\infty}^{\infty} w(x)e^{-ikx}\,dx = \frac{UA}{2\pi}e^{-|k|a}. \qquad (25)$$

Using (6), (14), (15), and (25) in the hydrostatic 2D limit, the source function can be computed from an inverse Fourier transform

$$S(x) = \frac{C_w U A}{2\pi}\int_{-\infty}^{\infty}\frac{e^{i|k|a}e^{ikx}\,dk}{[1 - i\hat{H}\,\text{sgn}(k)]}$$

$$= \left(\frac{C_w U A}{2\pi}\right)\left[\int_{-\infty}^{0}\frac{e^{ka}e^{ikx}\,dk}{(1 + i\hat{H})} + \int_{0}^{\infty}\frac{e^{-ka}e^{ikx}\,dk}{(1 - i\hat{H})}\right]. \qquad (26)$$

As $\hat{H}$ is independent of k in (26), the denominators can be brought outside the integrals. Evaluating (26) gives

$$S(x) = \left(\frac{C_w U A}{a}\right)\frac{a^2[1 - (x/a)\hat{H}]}{\pi(a^2 + x^2)(1 + \hat{H}^2)}, \qquad (27)$$
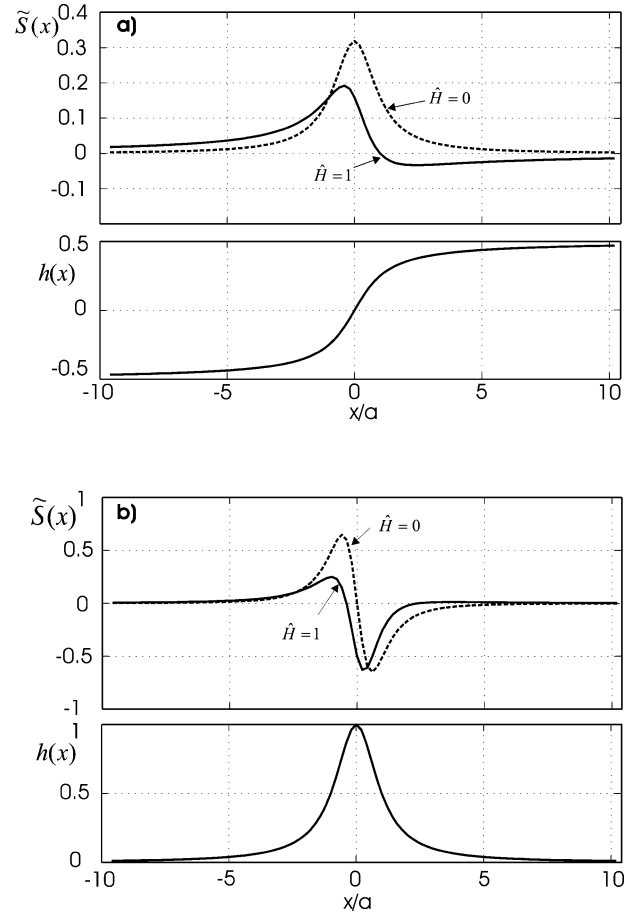

FIG. 2. The influence of wave dynamics on vertically integrated condensation. The cloud water source function $S(x)$ (nondimensional part) is shown for two values of nondimensional moist-layer depth; $\hat{H} = 0$ (dashed) and $\hat{H} = 1$ (solid). (a) Monotonic rise to a plateau (27). (b) Witch-of-Agnesi ridge (33). Wave dynamics reduces the source function, shifts it upstream, and modifies its shape.

where the square bracket carries the units of $S(x)$. According to (27), see Fig. 2a, one effect of $\hat{H}$ is to shift the condensation pattern upstream. The negative source region in (27), located at $x > a/\hat{H}$, is associated with a region of descending air in the mountain wave. Equation (27) satisfies (3) when $\hat{H} = 0$. The total source is

$$\overline{S} = \int_{-\infty}^{\infty} S(x)\,dx = C_w U A/(1 + \hat{H}^2). \qquad (28)$$

The second term in (27) makes no contribution to (28) as it is an odd function. The horizontal integral of the source function (28) is reduced from the raw value by the "dynamic precipitation efficiency"

$$\text{PE}_{\text{dyn}} = \frac{\overline{S}}{\overline{S}_{\hat{H}=0}} = (1 + \hat{H}^2)^{-1}. \qquad (29)$$

Using $\hat{H} = 1$, (29) gives $\text{PE}_{\text{dyn}} = 50\%$. It is interesting that, even with permanent lifting to a plateau, the con-

densation is significantly reduced due to the lack of penetration of the vertical motion field aloft.

d. Witch-of-Agnesi ridge

A third example is the classical Witch-of-Agnesi ridge shape

$$h(x) = \frac{Aa^2}{x^2 + a^2} \qquad (30)$$

with cross-section area πAa. Its Fourier transform is

$$\hat{h}(k) = \frac{Aa}{2} e^{-|k|a}. \qquad (31)$$

In the hydrostatic case (14), the source function can be computed from (16)

$$S(x) = \frac{iC_w UAa}{2} \int_{-\infty}^{\infty} \frac{ke^{-|k|a}e^{ikx}\, dk}{[1 - i\hat{H}\, \mathrm{sgn}(k)]}. \qquad (32)$$

Splitting the integral as before yields

$$S(x) = -\left(\frac{C_w UA}{a}\right)\left\{\frac{a^2[2ax + \hat{H}(a^2 - x^2)]}{(1 + \hat{H}^2)(a^2 + x^2)^2}\right\}, \qquad (33)$$

where the first pair of square bracket carries the units of $S(x)$. Equation (33) satisfies (3) when $\hat{H} = 0$. Compared to the raw upslope function (i.e., $\hat{H} = 0$), this formula shifts the condensation upstream and reduces its magnitude (Fig. 2b). It crosses zero and becomes negative, slightly upstream of the ridge peak. It also generates a small positive source region downwind, associated with ascent in a mountain wave aloft. This source function (33) has a zero net integral, but its upslope part can be isolated as

$$S_{\text{upslope}} = \int_{-\infty}^{0} S(x)\, dx = \frac{C_w UA}{(1 + \hat{H}^2)} \qquad (34)$$

to which the second term in (33) makes no contribution. When the nondimensional moist-layer depth is small, S_{upslope} reduces to the expected raw upslope value. The dynamical precipitation efficiency is again given by (29).

e. Isolated Gaussian hill

A problem with simple upslope models that lack airflow dynamics is that they take into account only terrain directly over or upwind of the test point. In fact, lateral terrain also has a significant influence on the condensation source function. The effect is captured in our transfer function (16). To illustrate the influence of lateral terrain, we consider an isolated elliptical Gaussian hill

$$h(x, y) = Ae^{-[(x/a_x)^2 + (y/a_y)^2]} \qquad (35)$$

with volume $\pi Aa_x a_y$. The aspect ratio for southerly winds is the ratio of the east–west width (a_x) to the

TABLE 1. Normalized upslope centerline condensation (36) influenced by hydrostatic airflow dynamics over a Gaussian hill.

	$\hat{H}$					
R	0	0.1	0.5	1	2	10
10 (wide)	1	0.99	0.83	0.60	0.33	0.06
2	1	0.96	0.72	0.50	0.28	0.05
1 (circular)	1	0.92	0.63	0.41	0.22	0.04
0.5	1	0.85	0.51	0.32	0.17	0.03
0.1 (narrow)	1	0.55	0.22	0.13	0.07	0.01

north–south width (a_y); that is, $R = a_x/a_y$. In the hydrostatic case, the source distribution generated by (13), (16) is independent of scale, but dependent on R and $\hat{H}$. To describe the influence of aspect ratio, we examine its influence on both the precipitation along the upwind centerline and over the full upslope region.

For southerly flow (i.e., along the y axis) we define the upslope centerline total source as

$$S_{\text{CL}} = \int_{-\infty}^{0} \max[S(x = 0, y), 0]\, dy. \qquad (36)$$

The upslope centerline value with no dynamics is $C_w VA$. Actual values of S_{CL}, determined from (36) using fast Fourier transform (FFT) evaluation of (13), (16), are shown in Table 1, normalized by the reference value (i.e., $S_{CL}/C_w VA$). From Table 1, we see that the circular hill ($R = 1$) and the wind-aligned ridge ($R < 1$) produce much less condensation on the centerline than a crosswind ridge ($R > 1$) of the same height. This effect can be explained by recalling how lateral structure in a mountain wave field influences vertical scale. For a wind-aligned ridge, the dominant terrain wavenumber vectors have a large ratio of the lateral to the windward components. According to (12) or (13), the role of the lateral component is to increase m, decreasing the vertical penetration of the forced ascent. Thus, the depth of the ascending air is only a fraction of the nominal depth (i.e., U/N_m). It follows that a crosswind ridge produces ascent that penetrates well aloft, while a wind-aligned ridge lifts only a shallow layer of air. If the moist layer is very thin, this rapid decay of vertical velocity (w) has little influence. For a typical value of $\hat{H} = 1$, however, the reduction by 3D effect is quite significant. For a circular hill ($R = 1$), the condensation over the upslope centerline is only 41% of the raw upslope value.

We now ask whether the reduction in centerline precipitation by dynamics (Table 1) might be compensated by increased precipitation on the rest of the upslope region. We define the total upslope condensation for southerly flow

$$S_{\text{upslope}} = \int_{-\infty}^{\infty} \int_{-\infty}^{0} \max[S(x, y), 0]\, dy\, dx, \qquad (37)$$

which has the reference value $\sqrt{\pi} C_w UaA$ for a circular

TABLE 2. Normalized total upslope condensation (37) for a circular Gaussian hill ($R = 1$).

$\hat{H}$	0	0.1	0.2	0.5	1.0	2.0	5.0	10.0
$S_{\text{upslope}}/\sqrt{\pi}\,C_w UaA$	1	1.01	0.99	0.87	0.63	0.35	0.14	0.07

Gaussian hill ($a = a_x = a_y$) with $\hat{H} = 0$. The normalized values of S_{upslope} are given in Table 2 as a function of nondimensional moist layer depth. With $\hat{H} = 1$, the total upslope condensation has dropped to 63% of the raw "no-dynamics" value. Tables 1 and 2 show that both centerline and total upstream condensation are reduced by dynamics. The total upslope condensation is reduced less due to lateral spreading of the forced ascent.

The effect of lateral spreading is also found when the wind blows through a mountain pass. While the local gap-forced ascent may be zero in such a case, the hills on either side produce ascent above the gap. If the gap is narrow and $\hat{H}$ is one or larger, the gap will experience nearly as much precipitation as the adjacent hill slopes.

f. Influence of the Coriolis force

Until now we have neglected the influence of the Coriolis force. This neglect is consistent with our focus on relatively small horizontal scales from 100 m to 100 km. Other assumptions of our model break down at scales of 200 km and larger, where the Coriolis force begins to dominate the dynamics. For example, the assumption of uniform background flow or the neglect of surface evaporation would fail at synoptic scales. Furthermore, the focus of our study, the dynamic and cloud-delay controls on precipitation, are not very important at the larger scales. The vertical penetration of broad-scale uplift is substantial and the cloud processes are relatively quick for very broad scale terrain.

The penetration of ascent can be estimated for large-scale flows using the quasi-geostrophic expression for the vertical wavenumber

$$m = \frac{iN_m}{f}(k^2 + l^2)^{1/2} \qquad (38)$$

(Queney 1947; Smith 1979). According to this formula, the penetration depth is approximately $d = fa/N_m$. If $f = 10^{-4}$ s^{-1}, $a = 500$ km, and $N_m = 0.005$ s^{-1}, the penetration depth is 10 km, well in excess of the typical moist layer depth.

4. Downslope evaporation

In this section, we describe how the linear model determines precipitation efficiency by treating downslope evaporation.

a. Formulation

We now consider the role of negative source regions (i.e., evaporation) associated with descent. Negative source regions were encountered in all the examples in section 3, even when the terrain rises monotonically to a plateau (24). Negative source regions in orographic flow could only be avoided if the background condensation rate (S_∞) were larger than the largest negative orographic perturbation.

In S03 and in section 2, only positive values of the source term were allowed, according to the truncation

$$S_{\text{trun}}(x, y) = \max(S, 0). \qquad (39)$$

The time-delay algorithm (5) spreads the condensed water downwind, independent of local terrain there. The influence of downslope regions is thereby neglected. According to (39) an isolated ridge [e.g., (30)] gives the same total precipitation as a long plateau [e.g., (24)] of the same height. By neglecting downslope evaporation in this way the upslope-time-delay model overpredicts the precipitation in valleys and overpredicts the total precipitation. If (39) is applied to the source function, negative precipitation values never arise. Recall that the delay algorithm (5) generates no negative values if the source function is always positive.

A possible evaporation scenario is illustrated in Fig. 1. In Fig. 1a, the sum of the two uplifts exceeds the net uplift (i.e., $S_1 + S_2 > S_3$). In cases with repeated uplift, the sum of sources can even exceed the incoming flux (i.e., $S_1 + S_2 > F$). If the total condensate falls immediately to the ground or drifts without evaporation, the model precipitation can exceed the influx (i.e., $P_1 + P_2 > F$)—an unphysical result. In reality, some fraction of S_1 must evaporate over the next downslope region to allow condensation on the next uplift. In Fig. 1b, smooth ascent guarantees $S_3 < F$ and $P_3 < F$ without evaporation.

To give more realism to the model, we seek a way to represent the effect of descent while avoiding negative values of precipitation. The simplest algorithm that captures this effect is a truncation of negative precipitation values, replacing (39) with

$$P_{\text{trun}}(x, y) = \max(P, 0), \qquad (40)$$

where P includes the orographic and the background precipitation (P_∞). From (1), (2), and (4) we see that negative values for P can arise where descent ($S < 0$) has first driven q_c negative. Then, through the conversion term, q_s goes negative also while q_c is driven back toward zero. This sequence represents the evaporation of cloud water followed by the evaporation of hydrometeors. In cases when q_c can change sign, it is better to think of this quantity as the "degree of supersaturation." When positive, it represents the column density of condensed cloud water. When negative, it represents the degree of subsaturation, that is, the amount of rain-

water that could be evaporated to return q_c to zero. In (1) and (2), we use the same time scale τ_c to represent the conversion of cloud water to hydrometeors and the evaporation of hydrometeors by subsaturated air.

In cases with weak P_∞, rapid conversion and fallout and persistent descent and drying our linear "saturated" formulation becomes problematic. When $q_c < 0$ and $q_s \leq 0$, the conversion term in (1) continues to remoisten the air even though there are no hydrometeors to evaporate. The truncation (40) assigns $P = 0$ to all such scenarios.

The airflow formulation in section 3 is also problematic in persistent dry descending flow, as we used the moist stability in the wave dynamics (14). While Jiang showed that dry leeside descent had little influence on windward ascent on single hills, strongly dried air encountering a second hill will not be treated well by our model.

b. Sinusoidal terrain

The effect of truncation (40) on total precipitation can be illustrated in 2D with sinusoidal terrain (17) with no airflow dynamics. Including cloud time delays (5) and the source function (20), the precipitation pattern can be written

$$P(x) = C_w k U \, \text{Re}\left\{\frac{Aie^{ikx}[(1 - \beta_c\beta_f) - i(\beta_c + \beta_f)]}{(1 + \beta_c^2)(1 + \beta_f^2)}\right\} + P_\infty, \qquad (41)$$

where $\beta_c = Uk\tau_c$ and $\beta_f = Uk\tau_f$. This function is shifted downstream compared to the source function (20) and it has reduced amplitude. The truncation condition (40) keeps only the positive parts of the sine wave in (41). A cloud-physics precipitation efficiency can be defined as the ratio of the positive areas of the precipitation and source sine waves. From (20) and (41), if $P_\infty = 0$,

$$\text{PE}_{\text{cloud}} = [(1 + \beta_c^2)(1 + \beta_f^2)]^{-1/2}. \qquad (42)$$

Consider an example where $\tau_c = \tau_f = 1000$ s, $U = 10$ m s^{-1}, $\lambda = 20$ km, and the terrain wavenumber $k = 2\pi/\lambda = 2\pi/20\,000$ so that $\beta_c = \beta_f = 3$. The cloud efficiency (42) is $\text{PE}_{\text{cloud}} = 0.1$. This reduction in efficiency is due to the effect of downslope evaporation.

c. Triangle ridge

A better example of downslope evaporation using truncation (40) is an isolated ridge. For the present, we neglect the effect of airflow dynamics. We can compute the precipitation by convolving the Green's function with the source distribution according to

$$P(x) = \int_{-\infty}^{x} G(x, x')S(x') \, dx', \qquad (43)$$

where G is given by (7). For simplicity, we consider a triangle ridge of height A centered at $x = 0$ with total width $2d$. The cross-sectional area of the ridge is Ad. The reference source functions on the windward and leeward slopes are

$$S_{\text{ref}} = C_w U dh/dx = \pm c,$$

respectively, where $c = C_w UA/d$. For simplicity, we also set one of the time constants equal to zero so that the appropriate Green's function is (8). Using (8), (43), the sum of all the upwind sources gives an expression for the precipitation on the windward slope

$$P(x) = c[1 - e^{-(x+d)/U\tau}] \quad \text{for } -d < x < 0 \qquad (44)$$

while on the lee slope, summing positive and negative sources gives

$$P(x) = c[e^{-x/U\tau}(2 - e^{-d/U\tau}) - 1] \quad \text{for } 0 < x < d. \qquad (45)$$

Upwind and downwind of the hill, $P(x) = 0$. According to (45), the precipitation spills over the peak, reaching to the cutoff position

$$x_c = U\tau \ln(2 - e^{-d/U\tau}) < d. \qquad (46)$$

Integrating (44) from $x = -d$ to 0 and (45) from $x = 0$ to $x = x_c$ gives the area total precipitation ($\overline{P}$), which we normalize with the windward condensation. After some algebra

$$\text{PE}_{\text{cloud}} = \frac{\overline{P}}{\overline{S}_{\text{ref}}} = \frac{\overline{P}}{cd} = 1 - \frac{x_c}{d} = 1 - \frac{\ln(2 - e^{-d/U\tau})}{(d/U\tau)}. \qquad (47)$$

For broad mountains with fast cloud processes, $d/U\tau \gg 1$ and (47) becomes

$$\text{PE}_{\text{cloud}} \approx 1 - \frac{\ln(2)}{(d/U\tau)} \approx 1.$$

In the opposite limit, $d/U\tau \ll 1$, (47) gives

$$\text{PE}_{\text{cloud}} \approx \frac{d}{U\tau}.$$

So (47) agrees quantitatively with the FFT solution (5) under corresponding conditions; (47) also agrees qualitatively with the formula derived by Jiang and Smith (2003) for a box model

$$\text{PE}_{\text{cloud}} = 1/(1 + U\tau/d). \qquad (48)$$

5. Combined airflow dynamics, advection, time delays, and downslope evaporation

a. Mathematical properties and controlling parameters

The key advantage of the linear model is that the airflow dynamics and cloud time delays produce a simple multiplicative effect in Fourier space. Combining (5) and (16) gives

TABLE 3. Some symbols used in the model.

Name	Symbol	Typical range
Mountain width	a	0.1 to 100 km
Mountain height	A	100 to 1000 m
Horizontal wind components	U, V	1 to 100 m s^{-1}
Moist stability frequency	N_m	0 to 0.01 s^{-1}
Water vapor scale height	H_w	1 to 5 km
Conversion time	τ_c	200 to 2000 s
Fallout time	τ_f	200 to 2000 s
Lapse rate	γ	-1 to $-7°$C km^{-1}
Moist adiabatic lapse rate	Γ_m	-5 to $-9°$C km^{-1}
Uplift sensitivity factor	C_w	0.001 to 0.02 kg m^{-3}
Background precipitation rate	P_∞	0 to 5 mm h^{-1}
Intrinsic frequency	σ	0.01 to 0.0001 s^{-1}
Vertical wavenumber	m	0.01 to 0.0001 m^{-1}
Precipitation efficiency	PE	0 to 1
Drying ratio	DR	0 to 1

TABLE 4. Nondimensional control variables for orographic precipitation.

Symbol	Formula	Description
B	$N_m a/U$	Nondimensional mountain width
$\hat{H}$	$N_m H_w/U$	Nondimensional moist-layer depth
D_c	$U\tau_c/a$	Nondimensional conversion drift distance
D_f	$U\tau_f/a$	Nondimensional fallout drift distance

$$\hat{P}(k, l) = \frac{C_w i\sigma \hat{h}(k, l)}{(1 - imH_w)(1 + i\sigma\tau_c)(1 + i\sigma\tau_f)}, \quad (49)$$

that is, a "transfer function" relating the Fourier transform of the terrain $\hat{h}(k, l)$ and the precipitation field $\hat{P}(k, l)$. As before, the coefficient C_w is given by (A9). The first factor in the denominator of (49) describes airflow dynamics. The second and third factors describe cloud delays and advection. The reduction in precipitation efficiency due to downslope evaporation is not contained explicitly in (49), but is present when (40) is applied after the inverse Fourier transform.

The combined theory (49) contains a number of dimensional parameters and variables (see Table 3) and four nondimensional control parameters (Table 4). As the model is linear, the mountain height (A) appears as a coefficient rather than a control parameter.

An interesting property of (49) is that the dynamics and cloud-delay factors in the denominator have a similar form. The appearance of $i = \sqrt{-1}$ in each factor causes a phase shift of the solution, in addition to the amplitude change. The different sign in the dynamic and cloud factors is significant. The negative sign in the dynamics factor gives an upwind shift to the precipitation pattern while the positive signs in the cloud factors cause a downstream shift. These factors also differ significantly in the way that wavenumber enters the definitions of $m(k, l)$ and $\sigma(k, l)$. Note that the two cloud time scales, τ_c and τ_f, are mathematically analogous. When $m = \tau_c = \tau_f = 0$, (49) reduces to the standard upslope model with no airflow dynamics and no condensed water advection.

Upon combining the dynamical and cloud physics effects (49), the multiplicative property of precipitation efficiency is retained only for flow over sinusoidal terrain. For hydrostatic flow, the expression for the precipitation efficiency (42) becomes

$$\text{PE} = \overline{P}/\overline{P}(\hat{H} = \beta_c = \beta_f = 0)$$
$$= [(1 + \hat{H}^2)(1 + \beta_c^2)(1 + \beta_f^2)]^{-1/2}, \quad (50)$$

taking into account the influence of airflow dynamics. For other terrain shapes, the precipitation fields need to be inverted and summed to obtain PE.

In the remainder of this section, we will apply (49) to two idealized hill shapes to illustrate its properties: that is, a triangle ridge and a 3D Gaussian hill.

b. Triangle ridge

The triangle ridge is a useful example, as the raw upslope condensation rate is constant over the windward slope. Thus, it is easy to see modification caused by airflow dynamics. Some insight into the pure cloud physics effect for a triangle ridge was given by (47). The combined influence of full dynamics and cloud time delays [(13) and (49)] is shown in Fig. 3, with parameters: $T_0 = 280$ K, $\gamma = -5.8°$C km^{-1}, $U = 15$ m s^{-1} so $\Gamma_m = -6.5°$C km^{-1}, $N_m = 0.005$ s^{-1}, $\rho_{S_{\text{ref}}} = 7.4$ g m^{-3}, $H_w = 2500$ m. Also $A = 500$ m and $\tau_c = \tau_f = 1000$ s.

In both parts of Fig. 3, the effect of airflow dynamics is to reduce the total condensation and shift the maximum upwind, close to the "slope break" of the triangle ridge. The source term turns negative slightly upstream of the hill crest. The effect of cloud delay reduces the precipitation further and shifts the precipitation peak downstream. For the narrower ridge, the precipitation maximum (2.96 mm h^{-1}) is close to the hilltop. For the wider ridge, the maximum (2.33 mm h^{-1}) is on the windward slope, about two-thirds of the way toward the hill crest. For both ridges, there is downstream condensation in a lee wave, but leeside descent and evaporation prevent precipitation. Especially for the narrow ridge, the ratio of total precipitation to total raw upslope condensation is quite small.

c. Isolated Gaussian hill

The isolated circular Gaussian hill (35 with $a_x = a_y$) is useful for showing lateral spreading, downstream drift, and the mountain wave contribution. Recall that the pure role of airflow dynamics over the isolated Gaussian hill was discussed in section 3e. Combined effects are shown in Fig. 4.

In Fig. 4a, we see that the raw upslope precipitation is confined to the windward slopes. With airflow dynamics (Fig. 4b), the condensation is much more widespread in the upstream region. Strong negative condensation values are seen in a butterfly pattern downstream.
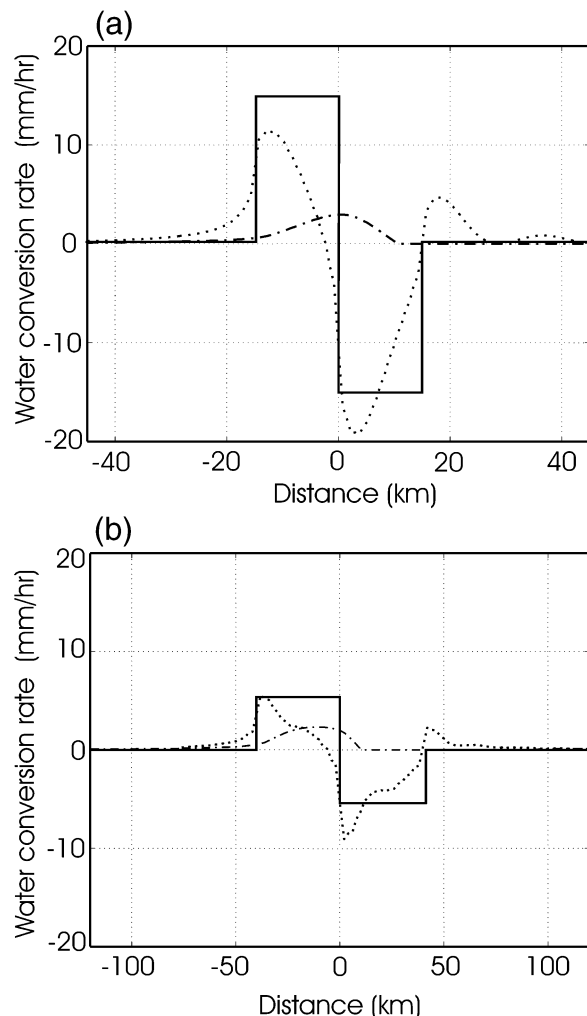
FIG. 3. Precipitation rates (mm h^{-1}) over a triangle ridge with three different assumptions: precipitation patterns with no dynamics or cloud delays (3) (solid); dynamics only (16) (dotted); dynamics and cloud delays (49) (dashed). Two mountain half-widths are shown: (a) $a = 15$ km, (b) $a = 40$ km. Parameters are $U = 15$ m s^{-1}, $N_m = 0.005$ s^{-1}, $T_0 = 280$ K, $H_w = 2500$ m, $\tau_c = \tau_f = 1000$ s, $A = 500$ m, $S_\infty = 0$. Note the great reduction in total precipitation caused by dynamics and cloud delays. The narrower hill has a precipitation maximum close to the hilltop and a lower overall precipitation efficiency.

By far the strongest negative values are just downstream of the peak due to mountain-wave-induced descent there. Farther downstream, a significant positive region of condensation is present associated with a wave cloud aloft.

After the cloud advection and truncation have been applied (Fig. 4c), the precipitation peak shifts to the hilltop. Some spillover is seen. A dry region is maintained on the lee slopes. A modest region of precipitation appears well downstream due to ascent in the mountain wave above the lee slope. Most of this wave-induced precipitation has been eliminated by the leeside drying. In the real world, there is little evidence for lee

wave precipitation, so we have cause to question this small remaining precipitation predicted by the linear model (see Bruintjes et al. 1994).

6. Scale dependence

A goal of this paper is to understand how the dominant processes and precipitation patterns and amounts vary with the horizontal topographic scale. For the current discussion, we examine full nonhydrostatic FFT evaluations of (49) for a 2D flow over a Gaussian ridge. In Fig. 5, we plot three "efficiency ratios" for fixed values of U, N_m, H_w, τ_c, τ_f, as the mountain width (a) varies from 100 m to 100 km. The ratios are

$$\mathrm{PE}_{\mathrm{dyn}} = \frac{\overline{S}_{\mathrm{dyn}}}{\overline{S}_{\mathrm{ref}}}, \qquad \mathrm{PE}_{\mathrm{cloud}} = \frac{\overline{P}}{\overline{S}_{\mathrm{dyn}}},$$

$$\mathrm{PE} = \mathrm{PE}_{\mathrm{dyn}}\mathrm{PE}_{\mathrm{cloud}} = \frac{\overline{P}}{\overline{S}_{\mathrm{ref}}}, \qquad (51)$$

where $\overline{S}_{\mathrm{ref}}$ is an area integral computed from (3), (40); $\overline{S}_{\mathrm{dyn}}$ and $\overline{P}$ are area integrals computed from the inverse FFT of (49) with (12) and (40). In the case of $\overline{S}_{\mathrm{dyn}}$ we set $\tau_c = \tau_f = 0$. The fixed parameters are $U = 15$ m s^{-1}, $N_m = 0.005$ s^{-1}, $H_w = 3000$ m, $\tau_c = 1000$ s, $\tau_f = 1000$ s. Unlike Table 1, the S_{dyn} in Fig. 5 includes the lee wave contribution. Note that, unlike sinusoidal terrain [e.g., (50)], the effects of pure airflow dynamics and pure cloud delay are not multiplicative. The ratio $\mathrm{PE}_{\mathrm{cloud}}$ in (51) describes the influence of cloud delays in the presence of airflow dynamics.

In Fig. 5, the ratio $\mathrm{PE}_{\mathrm{dyn}}$ rises quickly as width increases. For small-scale terrain, when $\sigma^2 > N_m^2$, the forced ascent decays quickly with height and little condensation occurs [see (12)]. At $a = 5$ km, a significant peak occurs associated with a near match between the mountain width and the buoyancy scale; that is, $a = U/N_m = 3$ km. This peak arises in part from good penetration and in part from the positive source contribution in a train of untrapped dispersive lee waves. These lee wave source regions do not cause precipitation as the condensed water from each cloud is advected quickly into a region of evaporation. Essentially they are "lee-wave lenticular clouds". This effect disappears and hydrostatic results obtain when the mountain width a exceeds 10 km for the chosen parameters, as orographic forcing at the resonant wavelength is much reduced.

We now discuss the curve for $\mathrm{PE}_{\mathrm{cloud}}$ in Fig. 5. For small-scale terrain, the precipitation efficiency from cloud processes is small. Condensed water from the upslope region is advected quickly to the lee side and evaporates before it has a chance to convert to hydrometeors and fall out (section 4). As the terrain scale increases, the time spent by a parcel in the upslope region increases. Progressively more of the condensed water has a chance to precipitate. For wide terrain, the value of $\mathrm{PE}_{\mathrm{cloud}}$ approaches unity as all the condensate precipitates.
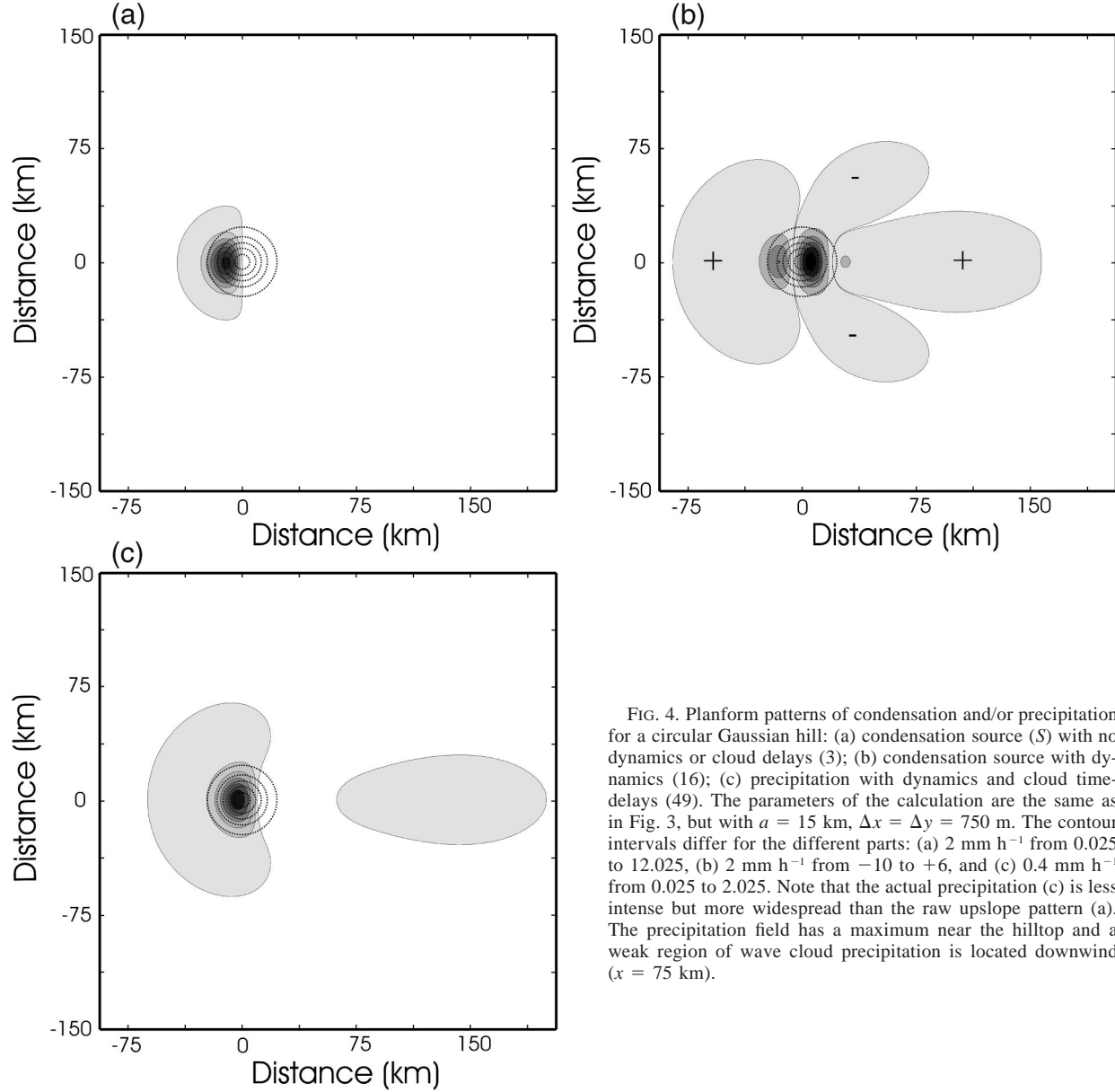
FIG. 4. Planform patterns of condensation and/or precipitation for a circular Gaussian hill: (a) condensation source (S) with no dynamics or cloud delays (3); (b) condensation source with dynamics (16); (c) precipitation with dynamics and cloud time-delays (49). The parameters of the calculation are the same as in Fig. 3, but with a = 15 km, $\Delta x = \Delta y$ = 750 m. The contour intervals differ for the different parts: (a) 2 mm h^{-1} from 0.025 to 12.025, (b) 2 mm h^{-1} from -10 to $+6$, and (c) 0.4 mm h^{-1} from 0.025 to 2.025. Note that the actual precipitation (c) is less intense but more widespread than the raw upslope pattern (a). The precipitation field has a maximum near the hilltop and a weak region of wave cloud precipitation is located downwind (x = 75 km).

The combined effect of airflow dynamics and cloud delay on PE is shown in Fig. 5; PE remains low until PE$_{cloud}$ begins to grow. For wide hills, PE$_{cloud} \approx 1$ and PE $\approx$ PE$_{dyn}$, so PE can never exceed the value PE$_{dyn}$ set by airflow dynamics. That is, if water does not condense, it cannot precipitate.

Changing the time-delay values will influence the precipitation efficiency, as shown in Table 5. As only the time constants are changed in the table, the quantity PE$_{dyn}$ does not change. In general, as the time delays are increased, the PE$_{cloud}$ decreases. More condensed water is advected onto the lee slope where it evaporates. In Table 5, note that the entry for $\tau_c = \tau_f$ = 1000 s agrees with Fig. 5.

An additional measure of precipitation efficiency is the ratio of precipitation to incoming water vapor flux, defined as the drying ratio (DR) by Smith et al. (2003). Using (51) and (A12),

$$\mathrm{DR} = \frac{\overline{P}}{F} = \left(\frac{\Gamma_m}{\gamma}\right)\left(\frac{A}{H_w}\right)\mathrm{PE}. \tag{52}$$

For example, from row six in Table 5, if PE = 0.61, (Γ_m/γ) = 2, A = 500 m, and H_w = 3000 m, then DR = 20%. For order of magnitude calculations, we can roughly combine hydrostatic dynamics (29) and box model advection (48) with (52) to obtain
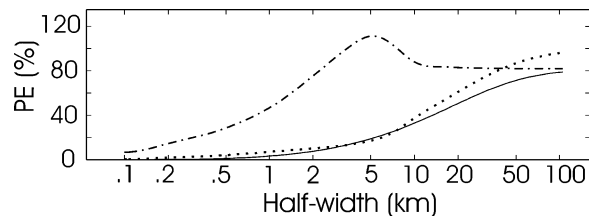
FIG. 5. Three efficiency ratios PE_{dyn} (dashed), PE_{cloud} (dotted), and PE (solid) as a function of mountain half-width for a Gaussian ridge according to the current linear model (12), (49). Parameters are the same as in Figs. 3 and 4.

TABLE 5. Influence of time constants on precipitation efficiencies for the Gaussian ridge (case $U = 15$ m s^{-1}, $N = 0.005$ s^{-1}, $a = 15$ km, $H_w = 3$ km, $S_\infty = 0$).

τ_c (s)	τ_f (s)	$PE_{dyn} = \overline{S}_{dyn}/\overline{S}_{ref}$ (%)	$PE_{cloud} = \overline{P}/\overline{S}_{dyn}$ (%)	$PE = \overline{P}/\overline{S}_{ref}$ (%)
0	250	82	96	79
0	500	82	84	70
0	1000	82	67	55
0	2000	82	47	39
250	250	82	91	75
500	500	82	74	61
1000	1000	82	51	42
2000	2000	82	31	25

$$\text{DR} = \frac{\overline{P}}{F} = \frac{\left(\dfrac{\Gamma_m}{\gamma}\right)\left(\dfrac{A}{H_w}\right)}{\left(1 + \dfrac{U\tau_c}{a}\right)\left(1 + \dfrac{U\tau_f}{a}\right)(1 + \hat{H}^2)}. \quad (53)$$

The drying ratio is a convenient measure of the non-linearity of the orographic precipitation system. A key assumption in linear theory is that the air remains near saturation everywhere. If the drying ratio is reasonably small (perhaps less than 0.3) this assumption may be useful. If DR exceeds 0.5 however, this assumption is less appropriate.

7. An application of the linear model

To illustrate the properties of the linear model, we present one example of a predicted precipitation pattern over real terrain. We select the Olympic Range in Washington State as it is compact, complex, and relatively well studied. It is one of the rainiest spots in North America, but with a definite rain shadow on the northeast side. Our intention in this section is not to test the model, but only to exhibit its behavior.

For the example, we consider a southwest wind with speed 15 m s^{-1} and a moist stability of 0.005 s^{-1}. The surface temperature and specific humidity are 280 K and 6.2 g kg^{-1}. The moist layer depth is 2.5 km. The cloud time delays are each 1000 s. The calculation was done on a large 1024 by 1024 grid with one kilometer resolution. The surrounding mountains were reduced with a Gaussian weighting function centered on the Olympics. Only a small portion of the computational domain is shown in Fig. 6. The calculation took about 8 seconds on a small workstation. The same computation could be done on a 256 × 256 grid in about 1 s.

In Fig. 6, the terrain has been smoothed with a 3000-m spectral filter for clarity of presentation, even though the terrain was only smoothed to 800 m for the FFT model run. The 6-h accumulated precipitation is shown in millimeters with a maximum value of about 26 mm just upwind of the highest peak, Mount Olympus (2428 m). Several features can be noted. Four tongues of high precipitation are associated with four southwestward directed ridges. Light precipitation is found well upstream

of the mountains, even over the sea. There is some spillover, but mostly the northeast lee slopes are dry. The model predicts that the high peaks in the northeast part of the massif collect no precipitation.

The sensitivity of these results to the model parameters can be estimated from the previous sections. The comparison with the raw upslope model ($m = \tau_c = \tau_f = 0$) is the most striking (not shown). It gives strong spikes of precipitation directly over each southwestern facing slope including those in the northeast corner of the range. Peak precipitation exceeds those in Fig. 6 by an order of magnitude.

8. Conclusions

We have developed a linear model of orographic precipitation including airflow dynamics, cloud time scales and advection, and downslope evaporation. The model is easy to apply to complex terrain. Only four steps are required: Fourier transform the terrain $h(x, y)$ to obtain $\hat{h}(k, l)$, multiply by the transfer function (49), perform an inverse Fourier transform, and apply the positive cutoff (40). The input parameters are P_∞, U, V, T_0, N_m, τ_c, τ_f, and a measure of vertical structure, N_m or γ. There is no need to smooth the terrain. The model includes crude representations of physical processes that provide the proper weights to the different scales, thus providing a theory of precipitation efficiency.

Several strong assumptions were made in the model formulation, for example, linear steady wave dynamics, near saturation, constant wind and moist stability with height and location, constant time delays, equal hydrometer growth and decay times, etc. The model only treats the vertically integrated condensed water. These simplifications could limit the accuracy and practical application of the model. Also, the model is unsuitable for unstable atmospheres.

Both the airflow and condensed water formulations become problematic in situations with fast conversion and fallout and persistent descent. The drying ratio (DR) can be a useful indicator of this breakdown in the theory.

We examined the role of scale in orographic precipitation using the linear model. Four natural atmospheric length scales appear: buoyancy scale, moist-layer thick-
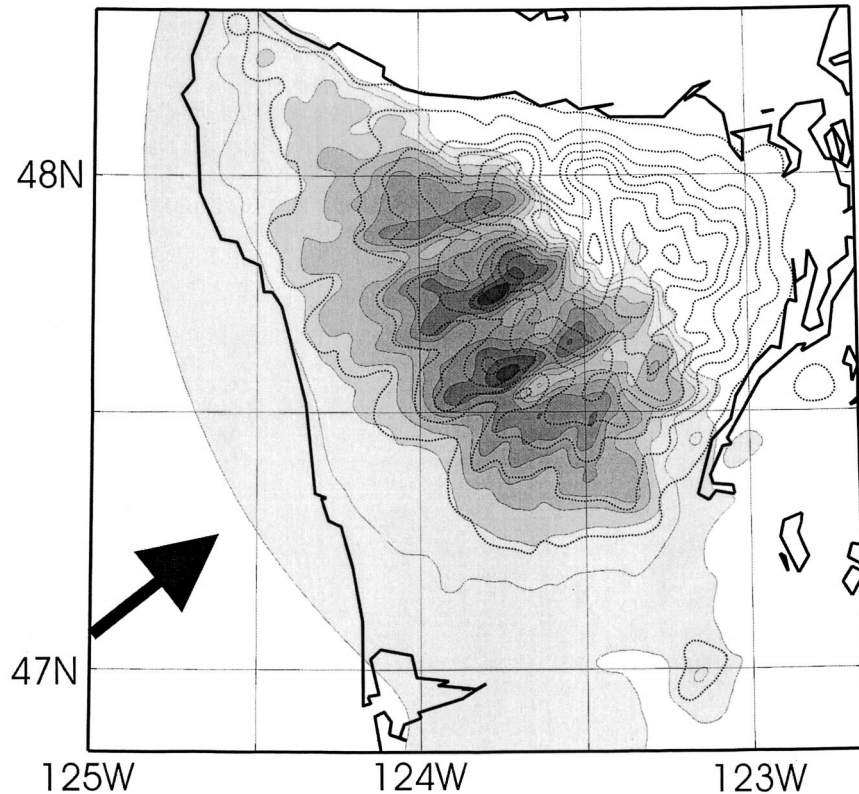
Fig. 6. A real-world application of the linear FFT model; the Olympic Mountains under a 15 m s^{-1} southwesterly airflow. The 6-h accumulated precipitation is shown shaded with a 2.5-mm contour interval. The maximum precipitation is 25.96 mm. The map projection is Lambert conformal. The atmospheric parameters in the model calculation are the same as in Figs. 3 and 4. The terrain is shown (dotted) with a 200-m contour interval. The coastline is shown with a dark solid line.

ness, and two drift distances. Both the pattern of precipitation and the total amount of precipitation are controlled by the ratios of mountain width to these inherent atmospheric scales.

The location of maximum precipitation is determined by a competition between the upstream shift caused by dynamics and the downstream shift caused by cloud delays. As mountain width decreases, the location of the maximum precipitation shifts from the windward slope to the hilltop. For narrow mountains and high wind speeds, spillover is possible.

The amount of precipitation is determined by the vertical penetration of the forced ascent relative to the depth of the moist layer and by the speed at which cloud droplets can convert and fall. Small-scale hills produce uplift that decays rapidly aloft, condensing little water. The ascent from broader hills penetrates much more using gravity wave dynamics. This penetration is also limited, however, and the condensation rate can be well below the raw upslope value.

The time delays from cloud processes also reduce precipitation. Here there is competition between the speed of conversion and fallout, and the time it takes for air parcels to reach the descending air in the lee. The cloud water or hydrometeors may drift to the lee side of a hill and evaporate before they can convert and fall to the ground. The combined effect of airflow dynamics and cloud delays may reduce precipitation by as much as an order of magnitude below the raw upslope model prediction.

We applied the linear FFT model to the Olympics under a southwest wind. The model ran quickly, with reasonable results. Quantitative testing of the linear model is under way and will be presented separately.

APPENDIX

Simple Thermodynamics

For use in the linear model, we need an approximate form of the thermodynamic equation for water that expresses the vertical profile with simple functions. The saturation water vapor density is

$$\rho_S = \frac{e_S(T)}{R_v T}. \qquad (A1)$$

We approximate the saturation vapor pressure according to the Clausius–Clapeyron equation

$$e_s(T) = e_{S_{\text{ref}}} e^{L\Delta T/R_v T_{\text{ref}}^2}, \qquad (A2)$$

where $e_{S_{\text{ref}}}$ and T_{ref} are the saturation vapor pressure and the temperature at the ground, and ΔT is the difference between the air temperature and reference temperature. In (A2), the latent heat is $L = 2.5 \times 10^6$ J kg^{-1} and the gas constant for vapor is $R_v = 461$ J kg^{-1} K^{-1}. If the environmental lapse rate is γ, the value of $\Delta T = \gamma z$. The vertical distribution of water vapor is [approximately, using (A1) and (A2) with $(T \approx T_{\text{ref}})$]

$$\rho_S(z) = \rho_{S_{\text{ref}}} e^{-z/H_w}, \qquad (A3)$$

where $\rho_{S_{\text{ref}}} = e_S(T_{\text{ref}})/RT_{\text{ref}}$ and

$$H_w = -\frac{R_v T_{\text{ref}}^2}{L\gamma}. \qquad (A4)$$

Using (A3) assuming that $\gamma < 0$, the column-integrated water vapor is $\rho_{S_{\text{ref}}} H_w$ and the horizontal flux of water vapor advected by a constant wind is

$$\mathbf{F} = \rho_{S_{\text{ref}}} H_w \mathbf{U}, \qquad (A5)$$

with x-component $F_x = \rho_{S_{\text{ref}}} H_w U$. Note that, if the ambient lapse rate approaches isothermal, the water vapor scale height grows and so does the column water vapor and flux, for a given surface value of vapor density. Positive values of lapse rate γ are not allowed here, as the column density of water vapor is not bounded.

The rate of change of saturation vapor density with temperature is [differentiating (A1) and using (A2)]

$$\frac{d\rho_S}{dT} = \rho_S\left[\left(\frac{L}{R_v T_{\text{ref}}}\right)\frac{1}{T_{\text{ref}}} - \frac{1}{T}\right] \approx \rho_S\left(\frac{L}{R_v T_{\text{ref}}}\right)\frac{1}{T_{\text{ref}}} \quad (A6)$$

to a good approximation as $L/(R_v T_{\text{ref}}) \approx 20$ for typical conditions: (A6) can be written as a function of height using (A3)

$$\frac{d\rho_S}{dT} = \rho_{S_{\text{ref}}}\left(\frac{L}{R_v T_{\text{ref}}}\right)\frac{1}{T_{\text{ref}}}e^{-z/H_w} = \frac{-\rho_{S_{\text{ref}}}}{\gamma H_w}e^{-z/H_w}. \quad (A7)$$

If the air is rising moist adiabatically at a rate $w(z)$, parcels cool at the rate $w\Gamma_m$. The local condensation rate is $w(d\rho_S/dT)\Gamma_m$. The column-integrated condensation rate is

$$S_{\text{ref}} = \frac{\rho_{S_{\text{ref}}}}{\gamma H_w}\int_0^\infty w\Gamma_m e^{-z/H_w}\, dz$$

$$= \left(\frac{C_w}{H_w}\right)\int_0^\infty w e^{-z/H_w}\, dz \qquad (A8)$$

if the moist lapse rate is assumed to be constant. In (A8),

$$C_w = \rho_{S_{\text{ref}}}\Gamma_m/\gamma \qquad (A9)$$

is the coefficient relating condensation rate to vertical motion. This coefficient captures the effect of environmental lapse rate on the condensation rate. The ratio of moist to environmental lapse rate is $\Gamma_m/\gamma > 1$ if the atmosphere is statically stable.

If the terrain-forced ascent, $w = U(dh/dx)$, is constant with altitude, (A8) gives

$$S_{\text{ref}} = C_w U \frac{dh}{dx}. \qquad (A10)$$

This formula agrees with Smith (1979) in the case of moist neutral conditions ($\gamma = \Gamma_m$). The total rate of condensation over the windward slope is, from (A10),

$$\overline{S}_{\text{ref}} = \int_{-\infty}^{x_{\text{top}}} S_{\text{ref}}\, dx = C_w UA, \qquad (A11)$$

where A is the mountain height and x_{top} is the location of the hilltop. The ratio of the condensation rate to incoming vapor flux is [using (A5) and (A11)]

$$\frac{\overline{S}_{\text{ref}}}{F_x} = \left(\frac{\Gamma_m}{\gamma}\right)\left(\frac{A}{H_w}\right) \qquad (A12)$$

independent of γ.

The wave dynamics in section 3 is controlled by the effective moist static stability given approximately by (Fraser et al. 1973):

$$N_m^2 = \frac{g}{T}(\gamma - \Gamma_m), \qquad (A13)$$

where Γ_m is an average moist adiabatic lapse rate. If we average Γ_m over the first kilometer, surface temperature of $T_0 = 253, 263, 273, 283,$ and 293 K give values of about $\Gamma_m = -9, -8, -7, -6, -5$ (°C km^{-1}), respectively. If, for example, the environmental lapse rate is $\gamma = -4$°C km^{-1} and $T_0 = 273$ K, (A13) gives $N_m = 0.0104$ s^{-1}. The ratio $\Gamma_m/\gamma = 1.75$. The water vapor scale height (A4) in this case is $H_w = 3.4$ km.

REFERENCES

Alpert, P., and H. Shafir, 1989: Meso-gamma-scale distribution of orographic precipitation: Numerical study and comparison with precipitation derived from radar measurements. *J. Appl. Meteor.,* **28,** 1105–1117.

Bader, M. J., and W. T. Roach, 1977: Orographic rainfall in warm sectors of depressions. *Quart. J. Roy. Meteor. Soc.,* **103,** 269–280.

Barcilon, A., and D. Fitzjarrald, 1985: A nonlinear steady model for moist hydrostatic mountain waves. *J. Atmos. Sci.,* **42,** 58–67.

——, J. C. Jusem, and S. Blumsack, 1980: Pseudo-adiabatic flow over a two-dimensional ridge. *Geophys. Astrophys. Fluid Dyn.,* **16,** 19–33.

Bruintjes, R. T., T. Clark, and W. D. Hall, 1994: Interactions between topographic airflow and cloud/precipitation development during the passage of a winter storm in Arizona. *J. Atmos. Sci.,* **51,** 48–67.

Collier, C. G., 1975: A representation of the effects of topography on surface rainfall within moving baroclinic disturbances. *Quart. J. Roy. Meteor. Soc.,* **101,** 407–422.

Daly, C., R. P. Neilson, and D. L. Phillips, 1994: A statistical–topographic model for mapping climatological precipitation over mountainous terrain. *J. Appl. Meteor.,* **33,** 140–158.

Durran, D. R., and J. B. Klemp, 1982a: On the effects of moisture on the Brunt–Väisälä frequency. *J. Atmos. Sci.,* **39,** 2152–2158.

——, and ——, 1982b: The effects of moisture on trapped mountain lee waves. *J. Atmos. Sci.,* **39,** 2490–2506.

Fraser, A. B., R. C. Easter, and P. V. Hobbs, 1973: A theoretical study of the flow of air and fallout of solid precipitation over mountainous terrain: Part I. Airflow model. *J. Atmos. Sci.,* **30,** 801–812.

Hobbs, P. V., R. C. Easter, and A. B. Fraser, 1973: A theoretical study of the flow of air and fallout of solid precipitation over mountainous terrain: Part II. Microphysics. *J. Atmos. Sci.,* **30,** 813–823.

Hutchinson, M. F., 1998: Interpolation of rainfall data with thin plate smoothing splines: II. Analysis of topographic dependence. *J. Geogr. Inf. Decis. Anal.,* **2,** 168–185.

Jiang, Q., 2003: Moist dynamics and orographic precipitation. *Tellus,* **55A,** 301–326.

——, and R. B. Smith, 2003: Cloud timescales and orographic precipitation. *J. Atmos. Sci.,* **60,** 1543–1559.

Kuligowski, R. J., and A. F. Barros, 1999: High-resolution short term quantitative precipitation forecasting in mountainous regions using a nested model. *J. Geophys. Res.,* **94,** 31 553–31 564.

Lalas, D. P., and F. Einaudi, 1973: On the stability of a moist atmosphere in the presence of a background wind. *J. Atmos. Sci.,* **30,** 795–800.

Miglietta, M. M., and A. Buzzi, 2001: A numerical study of moist stratified flows over isolated topography. *Tellus,* **53A,** 481–499.

Neiman, P. J., F. M. Ralph, A. B. White, D. E. Kingsmill, and P. O. G. Persson, 2002: The statistical relationship between upslope flow and rainfall in California's coastal mountain: Observations during CALJET. *Mon. Wea. Rev.,* **130,** 1468–1492.

Queney, P., 1947: Theory of perturbations in stratified currents with applications to airflow over mountain barriers. Dept. of Meteorology, Univ. of Chicago, Miscellaneous Rep. 23, 81 pp.

Rauber, R. M., 1992: Microphysical structure and evolution of a central Sierra Nevada orographic cloud system. *J. Appl. Meteor.,* **31,** 3–24.

Rhea, J. O., 1978: Orographic precipitation model for hydrometeorological use. Ph.D. thesis, Colorado State University, Dept. of Atmospheric Science, Atmospheric Science Paper 287, 198 pp.

Sawyer, J. S., 1962: Gravity waves in the atmosphere as a three-dimensional problem. *Quart. J. Roy. Meteor. Soc.,* **88,** 412–425.

Sinclair, M. R., 1994: A diagnostic model for estimating orographic precipitation. *J. Appl. Meteor.,* **33,** 1163–1175.

Smith, R. B., 1979: The influence of mountains on the atmosphere. *Advances in Geophysics,* Vol. 27, Academic Press, 87–230.

——, 2002: Stratified airflow over topography. *Environmental Stratified Flows,* R. Grimshaw, Ed., Vol. 3, *Topics in Environmental Fluid Mechanics,* Kluwer, 119–159.

——, 2003a: A linear upslope-time-delay model of orographic precipitation, mountain hydrology and water resources. *J. Hydrol.,* **282,** 2–9.

——, 2003b: Advection, diffusion and deposition from distributed sources. *Bound.-Layer Meteor.,* **107,** 273–287.

——, Q. Jiang, M. Fearon, P. Tabary, M. Dorninger, J. Doyle, and R. Benoit, 2003: Orographic precipitation and airmass transformation: An Alpine example. *Quart. J. Roy. Meteor. Soc.,* **129,** 433–454.

Wurtele, M. G., R. D. Sharman, and A. Datta, 1996: Atmospheric lee waves. *Annu. Rev. Fluid Mech.,* **28,** 429–476.